Can silver nanoparticles be useful as potential biological labels?

2008 Nanotechnology 19 235104

(http://iopscience.iop.org/0957-4484/19/23/235104)

Nanotechnology **19** (2008) 235104 (13pp) doi:10.1088/0957-4484/19/23/235104

Can silver nanoparticles be useful as potential biological labels?

Amanda M Schrand[1,2], Laura K Braydich-Stolle[1], John J Schlager[1], Liming Dai[2,3] and Saber M Hussain[1,3]

[1] Applied Biotechnology Branch, Human Effectiveness Directorate, Air Force Research Laboratory, Wright-Patterson AFB, OH, 45433-5707, USA
[2] Department of Chemical and Materials Engineering, University of Dayton, 300 College Park, Dayton, OH 45469-0160, USA

E-mail: Liming.dai@notes.udayton.edu and saber.hussain@wpafb.af.mil

Received 12 December 2007, in final form 19 February 2008
Published 6 May 2008
Online at stacks.iop.org/Nano/19/235104

Abstract

Silver (Ag) nanoparticles have unique plasmon-resonant optical scattering properties that are finding use in nanomedical applications such as signal enhancers, optical sensors, and biomarkers. In this study, we examined the chemical and biological properties of Ag nanoparticles of similar sizes, but that differed primarily in their surface chemistry (hydrocarbon versus polysaccharide), in neuroblastoma cells for their potential use as biological labels. We observed strong optical labeling of the cells in a high illumination light microscopy system after 24 h of incubation due to the excitation of plasmon resonance by both types of Ag nanoparticle. Surface binding of both types of Ag nanoparticle to the plasma membrane of the cells was verified with scanning electron microscopy as well as the internalization and localization of the Ag nanoparticles into intracellular vacuoles in thin cell sections with transmission electron microscopy. However, the induction of reactive oxygen species (ROS), degradation of mitochondrial membrane integrity, disruption of the actin cytoskeleton, and reduction in proliferation after stimulation with nerve growth factor were found after incubation with Ag nanoparticles at concentrations of 25 μg ml^{-1} or greater, with a more pronounced effect produced by the hydrocarbon-based Ag nanoparticles in most cases. Therefore, the use of Ag nanoparticles as potential biological labels, even if the surface is chemically modified with a biocompatible material, should be approached with caution.

(Some figures in this article are in colour only in the electronic version)

1. Introduction

The characteristics of an ideal nanomedical label include a lack of photobleaching or blinking, small size, no thermal perturbation or catalytic effects, stability in various environments, and biocompatibility. As optical labels, nanomaterials are typically classified as luminescent (i.e. encapsulated fluorescent dyes and quantum dots) or scattering (i.e. plasmon-resonant nanoparticles). Silver nanoparticles fall into the latter category of noble metal plasmon-resonant particles (i.e. Au, Ag, Pt, Pd) where the production of an optical signal occurs upon the excitation of surface plasmon resonances, which are collective oscillations of free electrons at the surface of metals (Lesniak *et al* 2005, Skebo *et al* 2007, Kumar *et al* 2007). These oscillations give rise to the intense colors of solutions of plasmon-resonant nanoparticles, such as silver and other metals/metal-oxides, which have recently been examined for agglomeration, uptake, and interaction in a variety of live cells with a high illumination system (Skebo *et al* 2007). The lateral resolution of such a system was experimentally determined to be approximately 60–90 nm, or a 6000× increase in magnification, in comparison to the 180 nm or less obtainable resolution in modern confocal instruments (Foster 2004, Vodyanoy 2005, Vainrub *et al* 2006). Therefore, taking advantage of both the intense plasmon-resonant properties of Ag nanoparticles and the enhanced resolution obtainable with the high illumination system in physiological solutions, studies on the interactions between Ag nanoparticles and live cells have been made possible.

[3] Authors to whom any correspondence should be addressed.

However, the use of silver nanoparticles in the imaging of neural tissue and cells, in particular, raises concerns over the possibility of contributing to neurodegenerative diseases (e.g. Parkinson's and Alzheimer's) due to their ability to produce reactive oxygen species and oxidative stress (Kedar 2003, Jendelova *et al* 2004). Indeed, studies in our laboratory have shown toxicity induced by silver nanoparticles in neuroendocrine cells, liver cells, and germ-line stem cells at concentrations between 5–100 μg ml^{-1} after 24 h of exposure (Hussain *et al* 2006, 2005, Braydich-Stolle *et al* 2005). In an effort to prevent the direct interaction between the nanoparticle surface and the cell and at the same time increase dispersion, the surface chemistry of metal and other nanoparticles, such as quantum dots or carbon nanotubes, can be engineered. This technique has proven to be an effective method preventing any inherent toxicity derived from the core nanomaterial (Dumortier *et al* 2006, Hoshino *et al* 2004, Chen *et al* 2005, Lesniak *et al* 2005, Wilhelm *et al* 2003, Gupta and Curtis 2004). The formation of a protective interfacial barrier between the metal core and cells is especially important for preventing damage to the surrounding healthy cells and tissues for applications where nanoparticles are targeted to certain cells such as photodynamic/thermolysis cancer cell destruction or the delivery of drugs/diagnostic agents (Gupta and Gupta 2005, Berry *et al* 2003, 2004, Jordan *et al* 1999). It has been shown that the incorporation of Ag nanoparticles into polymers (Balogh *et al* 2001, Yeo *et al* 2003, Jeong *et al* 2005, Chou *et al* 2005) or other materials for biomedical applications such as bone cement (Alt *et al* 2004) does not alter its toxic effect on bacteria and viruses. Other studies have found that the incorporation of Ag nanoparticles into polymers creates more stable dispersions in solution, which is important for applications such as imaging probes or for the deposition of thin films (Lesniak *et al* 2005, Balogh *et al* 2001, Suvorova *et al* 2005).

Therefore, from the perspective of both deliberate targeting of nanoparticles to the nervous system or accidental exposure and subsequent translocation, we chose a neuronal cell line, neuroblastoma (N2A), as our model *in vitro* system (Cool *et al* 1995, 1997). N2A cells were exposed for 24 h to two types of Ag nanoparticle, synthesized by different methods (hydrocarbons in plasma versus wet chemical synthesis with polysaccharides), for their potential use as biocompatible biological labels. The use of a consistent 24 h time-point provides sufficient time for nanoparticle interaction and uptake as well as the ability to detect biochemical changes in cellular function such as mitochondrial damage and reactive oxygen species production. In addition to standard cytotoxicity assays, the impact of Ag nanoparticle exposure on the neurotrophic factor, nerve growth factor (NGF), was examined because treatment with NGF has been shown to increase cell proliferation, survival, and differentiation of N2A cells (Blanco *et al* 2001). However, to assess the effect of NGF-induced proliferation a growth curve study was performed over a five-day period.

2. Materials and methods

2.1. Materials

Plasma gas synthesized Ag nanoparticles (Ag25) were a generous gift from Dr Karl Martin (Novacentrix, Austin, TX, formerly Nanotechnologies, Inc.). Polysaccharide-coated Ag nanoparticles (Ag25Disp) were a generous gift from Dr. Dan Goia (Clarkson University, Center for Advanced Materials Processing, Potsdam, NY). The two types of spherical Ag nanoparticle used in this study differed primarily in their surface chemical composition. The Ag25 nanoparticles were processed with hydrocarbons that prevent sintering, but leave a non-uniform hydrocarbon surface layer. The Ag25Disp nanoparticles were synthesized by the reduction of silver ions in solution by a polysaccharide (acacia gum), which leads to surface coating. Dosing solutions were prepared in cell culture media (Ham's F12 DMEM) without serum prior to each experiment.

2.2. Nanoparticle characterization

Concentrations and elemental compositions were determined with atomic absorption spectroscopy (AAS, Varian) and inductively coupled plasma-optical emission spectroscopy (ICP-OES, Thermo-Elemental IRIS Advantage DUO spectrometer) after silver nanoparticles were dissolved in nitric acid and diluted in water. Examination of the morphologies, surface coating, composition, crystal planes, and size distributions of the silver nanomaterials was performed with scanning electron microscopy (SEM, Hitachi S-4800, 15 kV) and transmission electron microscopy (TEM, FEI/Phillips CM200, 200 kV) with associated hardware for the collection of selected area diffraction patterns (SADPs) and energy dispersive x-ray (EDX, EDAX system) spectra. Samples were drop-cast onto formvar-coated TEM grids or aluminum SEM stubs and air dried before imaging. Information on mean size was calculated from a random field of view in addition to images that show the general morphology of the nanomaterials. Over 100 particles were counted and measured to determine the average sizes, standard deviations, and size distributions. Particle size and charge measurements in solution were determined with dynamic light scattering (DLS) and zeta potential measurements on a Malvern Instruments ZetaSizer, as previously described in Murdock *et al* 2008.

Further chemical analysis was performed to elaborate and confirm the elemental compositions, impurities, and surface chemistries with Fourier Transform infrared spectroscopy (FTIR, Perkin Elmer Spectrum One Fourier transform spectrometer), Raman (Renishaw inVia Raman microscope), and x-ray photoelectron spectroscopy (XPS, Surface Science Labs SSX-100 system). FTIR spectra were collected with Spectrum software (Perkin Elmer) over a range of 4000–450 cm^{-1}, scan speed of 0.2 cm s^{-1}, and at a spectral resolution of 4 cm^{-1}. Samples were prepared by drying the nanomaterials in liquid on a glass slide, scraping the dried residue, mixing with potassium bromide (KBr, Sigma), and then pressing into a pellet. A background spectrum was obtained before each measurement session using pure KBr at the same instrumental

conditions used for sample acquisition. Raman spectra were observed for Ag samples excited at 514 nm with a He–Ne laser. The experimental conditions were as follows: excitation power 50 mW, 60% laser power, five scans to improve the signal-to-noise ratio, and 20 s of exposure time with a 4 cm^{-1} slit width. Sample preparation consisted of drying several drops of the liquid suspension on a glass slide. The spectra were obtained in the range of 100–2000 wavenumber (cm^{-1}). XPS was performed with a monochromatic aluminum x-ray source with a nominal x-ray beam diameter of 600 μm. Sample preparation consisted of placing a drop of the two different Ag nanoparticle samples in water on a piece of clean Al foil, then allowing the water to evaporate at room temperature before measurements. The acacia gum powder (polysaccharide) was distributed on adhesive tape to form uniform and complete coverage. Microsoft Excel was used to display the XPS survey spectra as well as high resolution spectra for the elements of interest.

2.3. Cell culture

Murine neuroblastoma (N2A) cells, a neuronal phenotype, were a gift from Dr David Cool at Wright State University (Dayton, OH) (Cool *et al* 1995, 1997). Cells were seeded into T-75 flasks or 96-well plates and maintained in a 5% CO_2 incubator at 37 °C in Ham's F12 DMEM media (pH 7.4) with 10% normal FBS and 1% penicillin/streptomycin. After the desired growth period to 70% confluence, cell cultures were dosed with freshly prepared media without serum containing nanoparticles at concentrations ranging between 0–100 $\mu g\,ml^{-1}$ under conditions as previously described (Hussain *et al* 2005).

2.4. Microscopy of cells

Ultrahigh resolution images were obtained with the CytoViva^{TM} 150 Ultra Resolution Imaging system attachment (Aetos Technologies, Inc., Auburn, AL) after sealing, inversion, and oil immersion of slides containing cells, as previously described (Skebo *et al* 2007). Scanning electron microscope images of cells were taken on a FEI/Quanta 600 ESEM at 5 kV after fixation with 4% paraformaldehyde, dehydration through analytical grade 30–100% ethanol, mounting on aluminum stubs with double-sided carbon adhesive tape, and carbon coating. Associated energy dispersive x-ray spectra (EDS) were obtained with an EDAX Pegasus 4000 system and EDAX Genesis software. Fluorescent microscopy was used to demonstrate mitochondrial membrane permeability (Mit-E-Ψ^{TM} membrane permeability detection kit, BioMol) and cytoskeletal/nuclear morphology (Alexa-Fluor 555 Phalloidin, Molecular Probes and Prolong Gold Reagent with DAPI nuclear counterstain, Molecular Probes), as previously shown (Schrand *et al* 2007a). To determine if Ag nanoparticles were internalized by the N2A cells after 24 h, the cells were dosed with nanoparticles, then subsequently fixed with 2.5% glutaraldehyde/paraformaldehyde, post-fixed with 1% osmium tetroxide, dehydrated through 30–100% analytical grade ethanol, embedded in LR White resin, cured, and thin sectioned with an ultramicrotome (Leica Ultracut) to approximately 50 nm.

2.5. In vitro biocompatibility assessment

Mitochondrial function was evaluated spectrophotometrically by measuring the degree of mitochondrial reduction of the tetrazolium salt 3-(4,5-dimethylthiazol-2-yl)-2,5-diphenyltetrazolium bromide (herein referred to as the MTT assay) to an aqueous insoluble product (formazan crystals) by succinic dehydrogenase, which was extracted into a homogeneous dimethylsulfoxide solution (Carmichael *et al* 1987). Minor modifications to this assay were made as described elsewhere by Hussain and Frazier (2002), and an additional centrifugation step to remove nanoparticles from the solution before microplate reading was performed in order to avoid direct interference of the absorption values as found in previous studies (Schrand *et al* 2007a). The generation of intracellular reactive oxygen species (ROS) was determined using the fluorescent probe 2′,7′-dichlorohydrofluorescein diacetate (DCHF-DA) under a light controlled environment as described by Wang and Joseph (1999), with minor modifications as previously described by Hussain and Frazier (2002). The reactivity of the DCFH probe was evaluated with the reactive oxygen species generator, hydrogen peroxide, by serial dilutions of 30% H_2O_2 (Sigma) in PBS. The nerve growth factor (NGF, BD Biosciences) assay was performed by plating N2A cells at a concentration of 25 000 cells/well in a 96-well plate. 48 h after seeding, they were dosed with 25 $\mu g\,ml^{-1}$ of Ag25 or Ag25Disp. 24 h after dosing, the cells were treated with 20 $ng\,ml^{-1}$ of NGF daily. Each day, the cell proliferation was measured using the MTS assay (Promega) as follows: Day 0—dosing, Day 1—addition of NGF, MTS, Day 2—MTS, Day 3—MTS, Day 4—MTS, and Day 5—MTS.

2.6. Statistics

The above biochemical assays were performed in triplicate and the results were presented as mean ± standard deviation in comparison to control values. The data were subjected to statistical analysis by one-way analysis of variance (ANOVA) followed by Tukey–Kramer's procedure for multiple comparisons (pHStat Excel add-in) or two-way ANOVA statistical analysis (Microsoft® GraphPad Prism 4 followed by Bonferoni post hoc analysis). Furthermore, Bonferoni post hoc analysis was performed to determine differences between the different treatment groups. A value of $p < 0.05$ was considered significant and marked with an asterisk (*) on the graphs.

3. Results

3.1. Characterization of Ag nanoparticles

Variations in the properties of the two different Ag nanoparticles are attributed to differences in their synthesis methods and processing. According to the manufacturer, the hydrocarbon-processed Ag nanoparticles were synthesized out of a plasma gas, which includes silver and a mixture of other gases in a proprietary form including hydrocarbons. As the plasma cools, graphitic carbon and silver are both concurrently

Table 1. Summary of Ag size and charge characteristics.

Nanoparticle	TEM average size (nm)	DLS average size (in water) (nm)	DLS average size (in media) (nm)	Zeta potential (in water) (mV)
Ag25	27.5 ± 9.1	208	384	−26.2
Ag25Disp	26.0 ± 8.4	126	278	−39.4

formed, with the resulting hydrocarbons reducing the ability of the silver nanoparticles to sinter together. The approximately 2% amorphous carbon (confirmed with XRD and EDS) in the final product is not chemically bound to the silver, but rather surrounds it as a matrix to prevent agglomeration. In contrast to the hydrocarbon-processed Ag nanoparticles, the polysaccharide-coated Ag nanoparticles were produced through a reduction of silver ions in an aqueous solution by a naturally occurring polysaccharide polymer (MW $\sim$ 250 000). In this case, the Ag is reduced by the functional groups inserted on the extended polysaccharide chains. The nanoparticles formed are wrapped into the polymer and separated from the surrounding environment. A controlled subsequent degradation of the polymer ensures the formation of a continuous and adherent polysaccharide coating. The importance of the polysaccharide surface coating is to modify the interaction between the surface of the Ag nanoparticles and cells. For this reason, we chose to compare these two different types of Ag nanoparticle for their characterization, ability to act as biolabels, and biocompatibility.

The two types of Ag nanoparticle show similarities in their spherical morphologies, polydisperse sizes ranging from 9.9 to 51.9 nm, crystalline diffraction patterns, and predominantly silver elemental composition (figures 1(A)–(J)). Scanning electron micrographs of the two types of Ag nanoparticle show very few morphological differences (figures 1(A), (F)). The appearance of Ag25 (figure 1(A)) is somewhat more clustered compared to Ag25Disp (figure 1(F)), which can be attributed to the formation of large, dry powder aggregates for Ag25 nanoparticles compared to the synthesis and sample preparation of Ag25Disp in aqueous solution. The use of SEM reveals similarities between the size and morphology of the two different types of Ag nanoparticle, but cannot reveal the presence of surface hydrocarbons or the polysaccharide coating. However, bright-field TEM demonstrates the size, morphology, and presence of the surface coating on the Ag nanoparticles. For example, the lacy appearance of the amorphous carbon on and surrounding the Ag25 nanoparticles is shown in figure 1(B), denoted by the white arrows. The polysaccharide coating of Ag25Disp is also shown with bright-field TEM (figure 1(G), black arrows). Selected area diffraction patterns (SADPs) show the 111, 200, 220, and 113 planes in both samples, demonstrating the similar crystalline structures (figures 1(C), (H)). Measurement of 100 randomly selected individual nanoparticles measured from TEM images show that Ag25 range in size from 9.9 to 51.9 nm with the majority of the Ag25 nanoparticles being 25–30 nm, with an average size and standard deviation of 27.5 ± 9.1 nm (figure 1(D)). The majority of the Ag25Disp are 20–25 nm with a range of 11.8–47.9 nm and an average size and standard deviation of 26.0 ± 8.4 nm (figure 1(I)). However, there are slight differences in the EDX spectra, demonstrating elemental differences between the compositions of the Ag nanoparticles (figures 1(E), (J)). Because the hydrocarbon-processed Ag nanoparticles were synthesized in a powder form without a uniform surface coating, the surface areas exposed to air readily bind with sulfur as part of the oxidative corrosion process, known as tarnishing, and a peak for sulfur is shown in the EDX spectra of Ag25 (figure 1(E)). Another difference between the spectra of the two types of Ag nanoparticle used in this study was the increased C peak in Ag25Disp, which is attributed to the carbon-rich polysaccharide. The presence of Cu, and trace amounts of Fe and Co, in both spectra are from the elements present in the Cu alloy TEM grid. All of the data for electron microscopy and associated techniques was obtained under high vacuum and constitutes the size, morphology, electron diffraction, and composition analysis characteristics of the primary nanoparticles. However, once the Ag nanoparticles were introduced water or cell culture media, the sizes changed to approximately 4–8 times the primary size with further increases in size in cell culture media compared to water alone, resulting in average agglomerate sizes for the Ag nanoparticles from between 100–400 nm (table 1). A more detailed analysis of the surface chemical groups present on the Ag nanoparticle surfaces can contribute to understanding the mechanism of toxicity or biocompatibility because these surfaces will come into direct contact with the cells; see below.

The chemical properties of nanoparticles are critical for understanding the possible attractive or repulsive forces of functional groups that comprise the interfaces between nanoparticles and cells. In this study, a combination of FTIR, Raman, and x-ray photoelectron spectroscopy (XPS) was performed to characterize the nanoparticles. The FTIR spectrum of both types of Ag nanoparticle show strong absorption peaks at 3430 cm^{-1} and weaker intensity peaks at approximately 1630 cm^{-1}, which can be ascribed to the O–H vibrational mode (figure 2(A)). The rich presence of hydroxyl groups bound to the surface of the Ag nanoparticles and broadening of the peaks due to hydrogen bonding are well known phenomena of hydrated compounds (Hummel 1982, Coates 2000). The presence of additional peaks for Ag25Disp at $\sim$2900, 1054, and 786 cm^{-1} represent C–H stretch and C–O groups well known for polysaccharides (Bellamy 1975). The Raman spectra support the greater presence of carbonaceous coating on the polysaccharide-coated Ag25Disp sample (figure 2(B)). As shown in figure 2(B), there are two large peaks at approximately 1590 and 1360 cm^{-1} compared to much smaller scatterings for the hydrocarbon-processed Ag25 sample.

X-ray photoelectrons are capable of detecting chemical compositions of the very outermost layers (e.g. 1–3 nm) of the two different Ag nanoparticle samples (figures 2(C)–(E)). In

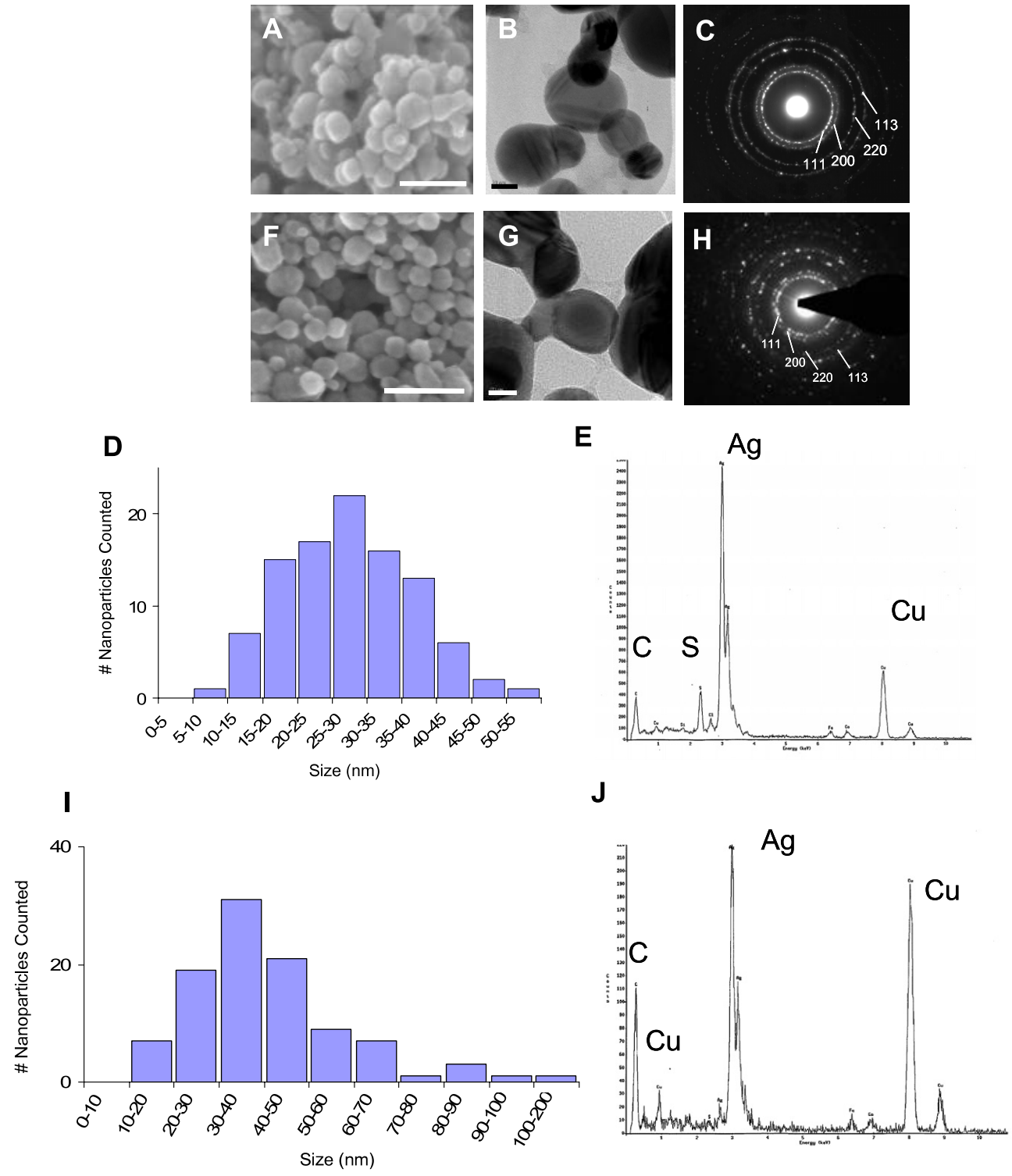

Figure 1. Electron microscopy characterization of hydrocarbon-processed Ag25 and polysaccharide-coated Ag25Disp nanoparticles. ((A)–(E)) Ag25 and ((F)–(J)) Ag25Disp. ((A), (F)) Scanning electron microscopy images with scale bars 100 nm, ((B), (G)) Transmission electron microscopy images with scale bars 20 nm, ((C), (H)) Selected area diffraction patterns (SADPs), ((D), (I)) Ag nanoparticle size distribution taken from 100 nanoparticles counted in TEM, and ((E), (J)) energy dispersive x-ray spectra.

the Ag25 sample, Ag is resolved with some oxygen and carbon present due to the hydrocarbon processing (figure 2(C)). In contrast, the polysaccharide-coated Ag25Disp (figure 2(D)) has a much lower C/O ratio compared to the Ag25 due to the presence of many C–O, C=O, and O–C–O groups on the polysaccharide. However, the Ag/O and Ag/C ratios are much lower for the polysaccharide-coated Ag nanoparticles compared to the Ag25 nanoparticles because they are covered with polysaccharide thicker than 3 nm, which masks the detection of the underlying Ag (table 2). The detection of

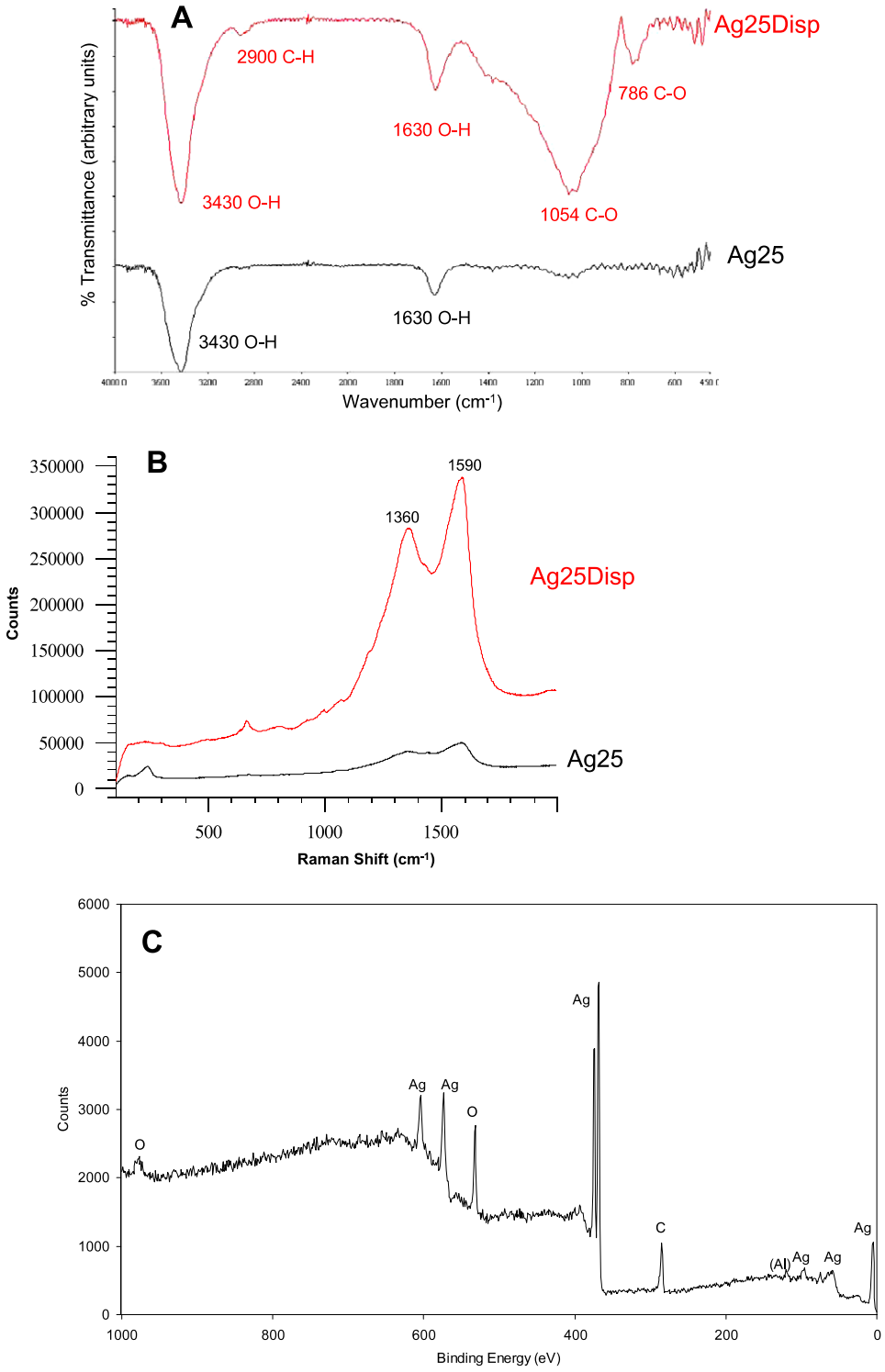

Figure 2. Chemical analysis of Ag nanoparticles with FTIR, Raman, and XPS techniques. (A) FTIR spectra of Ag nanoparticles demonstrating differences in the chemical make up of hydrocarbon-processed and polysaccharide-coated Ag nanoparticles. The upper spectrum is Ag25Disp, with a large and broad C–O peak characteristic for the polysaccharide coating, and the lower spectrum is Ag25, which lacks this peak. (B) Raman spectra demonstrating differences in the chemical surface states of hydrocarbon-processed and polysaccharide-coated Ag nanoparticles. The upper spectrum is Ag25Disp, showing two prominent C-based peaks, and the lower spectrum is Ag25, with low scattering. (C) Ag25; (D) Ag25Disp; and (E) polysaccharide. Notice the increased C/O ratio and decreased Ag/O and Ag/C ratios in Ag25Disp due to the polysaccharide coating in (D).

sodium and a greater amount of nitrogen was also found on the Ag25Disp sample. The N 1s binding energy would be consistent with an amine (NH_2 or NH). The polysaccharide (acacia gum) alone shows the presence of predominantly C and O with a lower amount of N. Specifically, there is an intense C–O carbon component due to C–OH or C–O groups

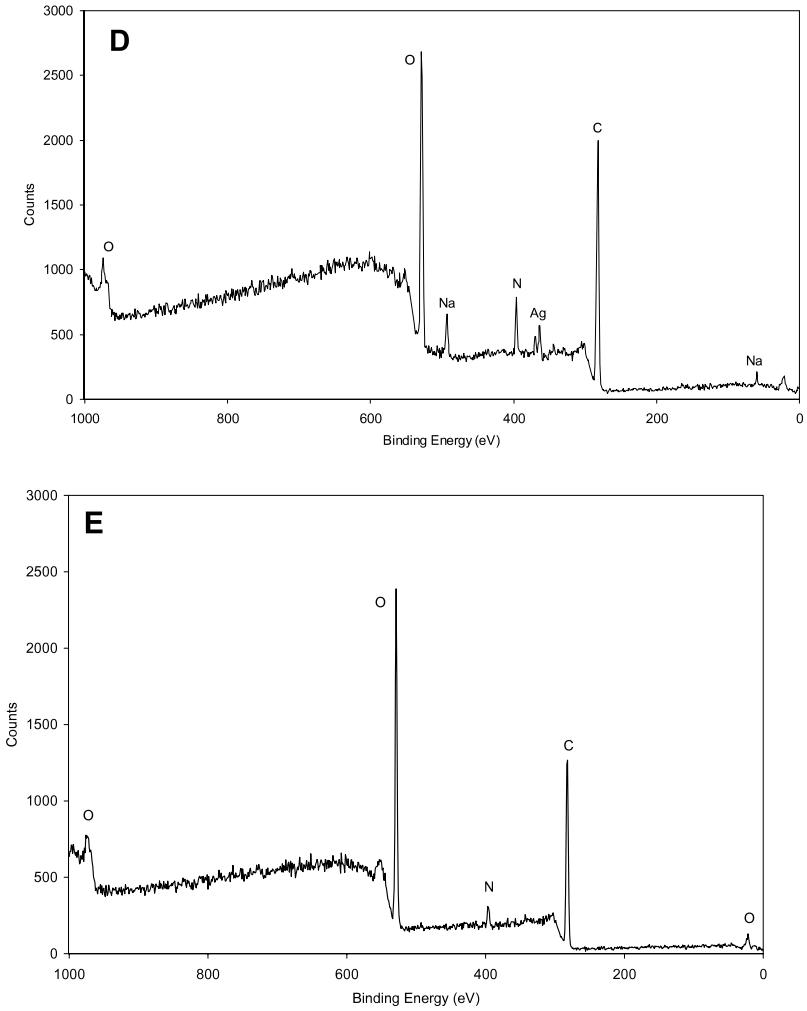

Figure 2. (Continued.)

Table 2. Approximate at.% surface compositions of Ag nanoparticles and polysaccharide powder determined by x-ray photoelectron spectroscopy.

Sample	C			O	Na	N	Ag	Al	S
	C=O, OCO	C–O	C–H, C						
Ag25	4.9	7.6	28	33.5	—	—	22.4	3.7	—
Ag25Disp	12.7	24.9	22.5	27.6	4.7	6.2	1.4	—	—
Acacia gum (polysaccharide)	10.8	38.1	8.8	39.1	—	3.1	—	—	—

and a low level of nitrogen due to the protein component in the polysaccharide.

3.2. Microscopy of cells after incubation with Ag nanoparticles

Neuroblastoma cells were untreated or incubated with Ag nanoparticles for 24 h before visualization with high illumination light microscopy or scanning electron microscopy for observations of morphological changes and Ag nanoparticle binding (figure 3). Control neuroblastoma cells prepared for imaging with high illumination light microscopy typically appear elongated in morphology with a diffuse blue tint characteristic of illumination and reflectance from endogenous scattering associated with internal cellular organelles such as mitochondria, endosomes, or vesicles (figure 3(A)). Similarly, cells that were incubated with 25 μg ml^{-1} of Ag25Disp or Ag25 nanoparticles for 24 h, then washed with cell culture media to remove unbound nanoparticles, show similar cell morphologies to the control cells (figures 3(B)–(C)). The Ag nanoparticles are brightly illuminated and distinctly rounded nanoparticle agglomerates that were noticeably distinguishable from the background cellular illumination with a strong interaction to the cell membrane and neurites (figures 3(B)–(C)). The Ag25

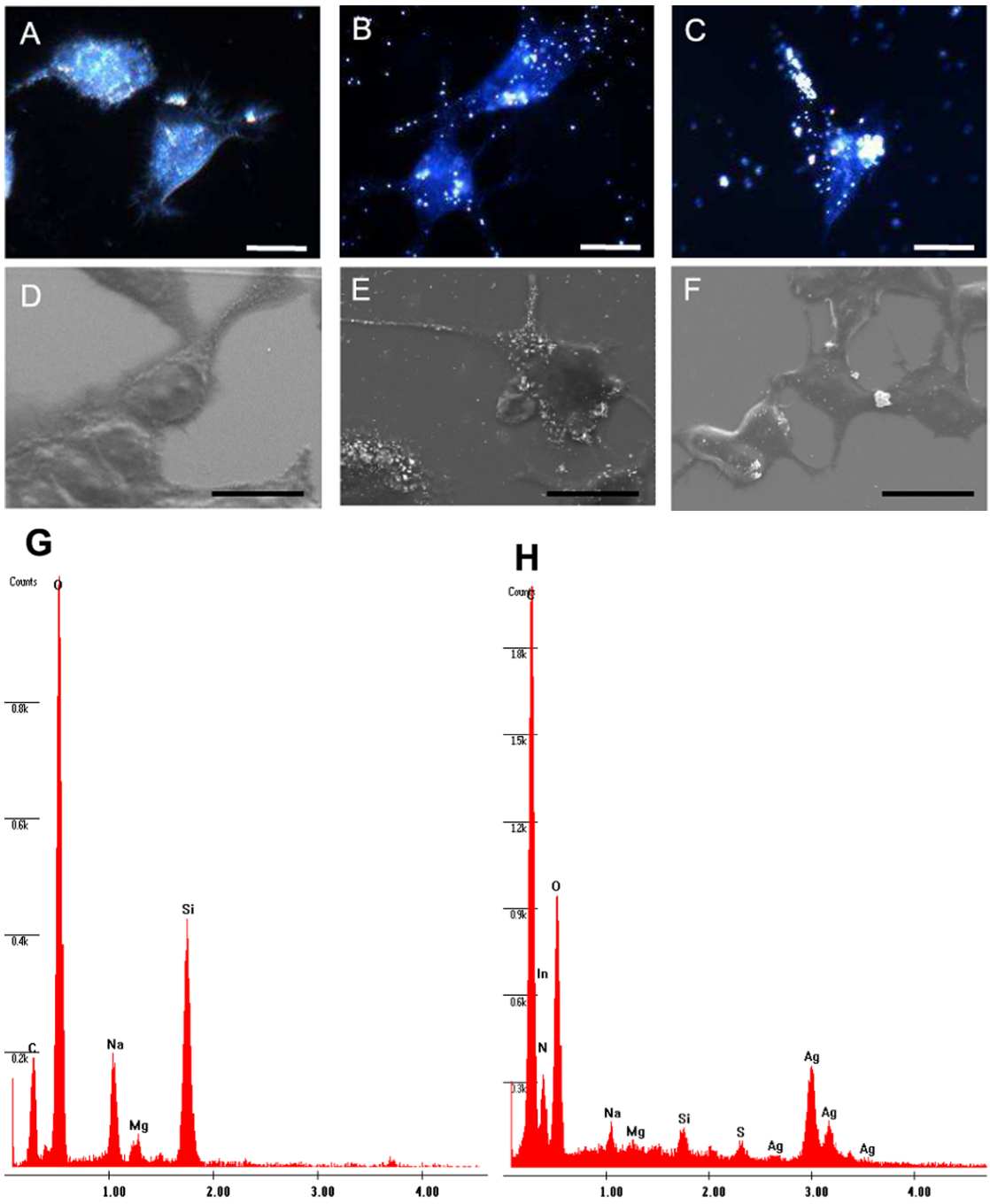

Figure 3. ((A)–(C)) High illumination light microscopy of (A) control N2A cells; (B) 25 μg ml^{-1} Ag25Disp; (C) 25 μg ml^{-1} Ag25. ((D)–(F)) Scanning electron microscopy of (D) control N2A cells; (B) 25 μg ml^{-1} Ag25Disp; (C) 25 μg ml^{-1} Ag25. ((G)–(I)) Energy dispersive x-ray analysis of (G) control N2A cells; (H) cells incubated with Ag25Disp; and (I) cells incubated with Ag25. The scale bars are 20 μm.

nanoparticles (figure 3(C)) appear to be more agglomerated than the Ag25Disp nanoparticles (figure 3(B)). Although this procedure of nanoparticle incubation and washing before high illumination imaging is a quick and convenient technique that does not require the use of extra chemicals for sample preparation, it allows the imaging of interactions between nanoparticles and live cells. However, it is not certain whether the nanoparticles are solely located on the surface of the cells or if they have been internalized, and what long-term effects the nanoparticles may have on cellular function.

To verify if the Ag nanoparticles were truly attached to the outer portion of the plasma membrane, the cells were examined with scanning electron microscopy and the presence of the Ag nanoparticles was confirmed with energy dispersive x-ray analysis (EDS). The control cells lacked the presence of any higher atomic contrast materials on the surface with an overall gray appearance (figure 3(D)). The lack of Ag was also verified with EDS, which showed only the presence of C, O, Na, Mg, and Si. The Si signal is from the underlying substrate. However, the Ag nanoparticles on the surface of

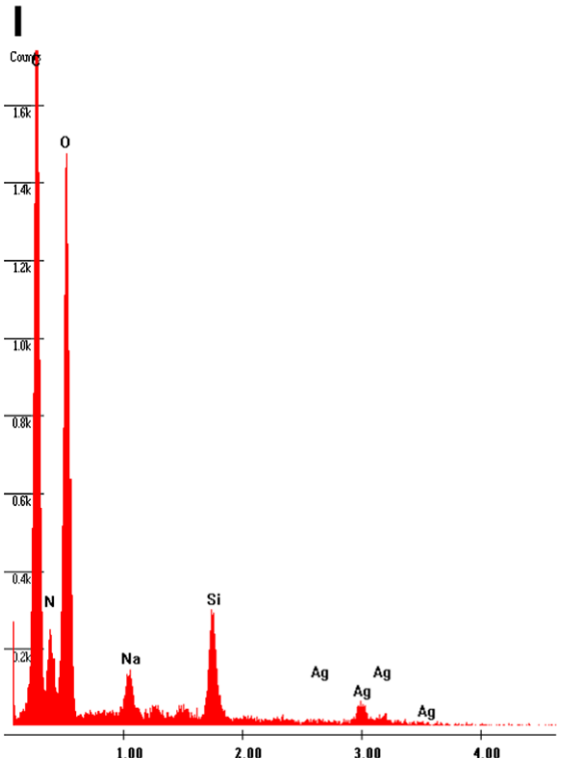

Figure 3. (Continued.)

the dosed cells were easily distinguishable from any sample preparation artifacts and cellular membrane irregularities due to their higher atomic contrast than the carbonaceous cellular material (figures 3(E)–(F)). In the cells dosed with 25 μg ml^{-1} of Ag25Disp nanoparticles (figure 3(E)), there was a more uniform surface binding of the Ag nanoparticles compared to the Ag25 nanoparticles, which had large aggregates up to 5 μm in size (figure 3(F)). The presence of Ag was found for both cell samples dosed with Ag nanoparticles in addition to the elements present in the control sample (figures 4(H)–(I)). One difference between the Ag25 and Ag25Disp nanoparticles was the presence of a S peak in Ag25Disp, which is due to an added stabilizing agent (Daxad), which is a sodium salt of a high-molecular-weight naphthalene sulfonate formaldehyde condensate (Sondi *et al* 2003).

To determine if either type of Ag nanoparticle was internalized by the cells after 24 h, the cells were incubated with 25 μg ml^{-1} of Ag25 or polysaccharide-coated Ag nanoparticles, embedded in LR White resin, thin sectioned with an ultramicrotome, and examined with transmission electron microscopy (TEM). Silver nanoparticles were found in membrane-bound intracellular vacuoles that appear to be endosomes by their size, shape, and location near the surface of the plasma membrane after 24 h (figure 4). Endosomes are typically acidic reservoirs that are responsible for transporting material for further degradation by lysosomes (Alberts *et al* 2004). Inside the intracellular compartments, individual Ag25 nanoparticles ranging in size from 15–50 nm were found in relatively loose aggregates (figure 4(B)). In contrast, polysaccharide-coated Ag25Disp nanoparticles appeared aggregated once inside the cell (figures 4(C)–(D)). Multiple images suggest that the polysaccharide coating is maintained after 24 h of incubation with cells and after internalization by the appearance of a lower contrast matrix surrounding multiple Ag25Disp nanoparticles.

Because both types of Ag nanoparticle were internalized after 24 h, subcellular effects were further examined. It is hypothesized that the small size of nanoparticles may allow their translocation into critical organelles such as mitochondria (Foley *et al* 2002) or that they may interact with cellular proteins of the cytoskeleton such as actin (Schrand *et al* 2007a). Therefore, after cells were incubated with Ag nanoparticles for 24 h, fluorescent microscopy was used to examine the effect of the nanoparticles on mitochondrial membrane permeability and cytoskeletal architecture (figures 4(E)–(L)). The use of the Mît-E-Ψ^{TM} fluorescent reagent allows the visualization of healthy mitochondria, which aggregate the dye and emit red fluorescence, compared to cells with damaged mitochondrial membranes where the dye fluoresces green in the cytoplasm (figures 4(E)–(H)). Aggregation and retention of the mitochondrial dye inside healthy control cells is shown in figure 4(E) and leakage of the dye in cells incubated with the positive control CdO is shown in figure 4(H). A representative image of cells incubated with 25 μg ml^{-1} of Ag25 nanoparticles (figure 4(G)) showed reduced mitochondrial membrane integrity compared to Ag25Disp (figure 4(F)) as indicated by predominantly green dispersion of the dye in the cytoplasm compared to punctuate areas of red and green overlap. Fluorescent staining and microscopy of the actin cytoskeleton and nuclei of cells incubated with or without Ag nanoparticles showed a similar trend in subcellular disruption (figures 4(I)–(L)). Cells incubated with Ag25 nanoparticles (figure 4(K)) or the positive control CdO (figure 4(L)) did not retain an intact cytoskeleton in comparison to control cells (figure 4(I)) or cells incubated with Ag25Disp nanoparticles (figure 4(J)).

3.3. Biocompatibility assessment of Ag nanoparticles

It was hypothesized that the polysaccharide synthesis and subsequent surface chemistry changes would increase the biocompatibility of Ag nanoparticles. Therefore, in order to assess the differences in the biocompatibility of the two types of Ag nanoparticle, an MTT assay was performed (figure 5(A)). Cells incubated with the positive control silver nitrate ($AgNO_3$) showed great toxicity at a low concentration of 0.1 μg ml^{-1}. By comparison, cells incubated with Ag25Disp nanoparticles maintained higher average viabilities than Ag25 nanoparticles at concentrations from 0.5–25 μg ml^{-1}. However, both types of Ag nanoparticle significantly reduced cell viability after 24 h of incubation at 25–100 μg ml^{-1} concentrations. The biocompatibility of the polysaccharide alone was tested at concentrations from 100 to 10 000 ng ml^{-1} (10 μg ml^{-1}) and shows no significant difference from the control (figure 5(B)). Therefore, these MTT viability results support the prior fluorescent microscopic images demonstrating a greater biocompatibility of the Ag25Disp nanoparticles compared to the Ag25 nanoparticles.

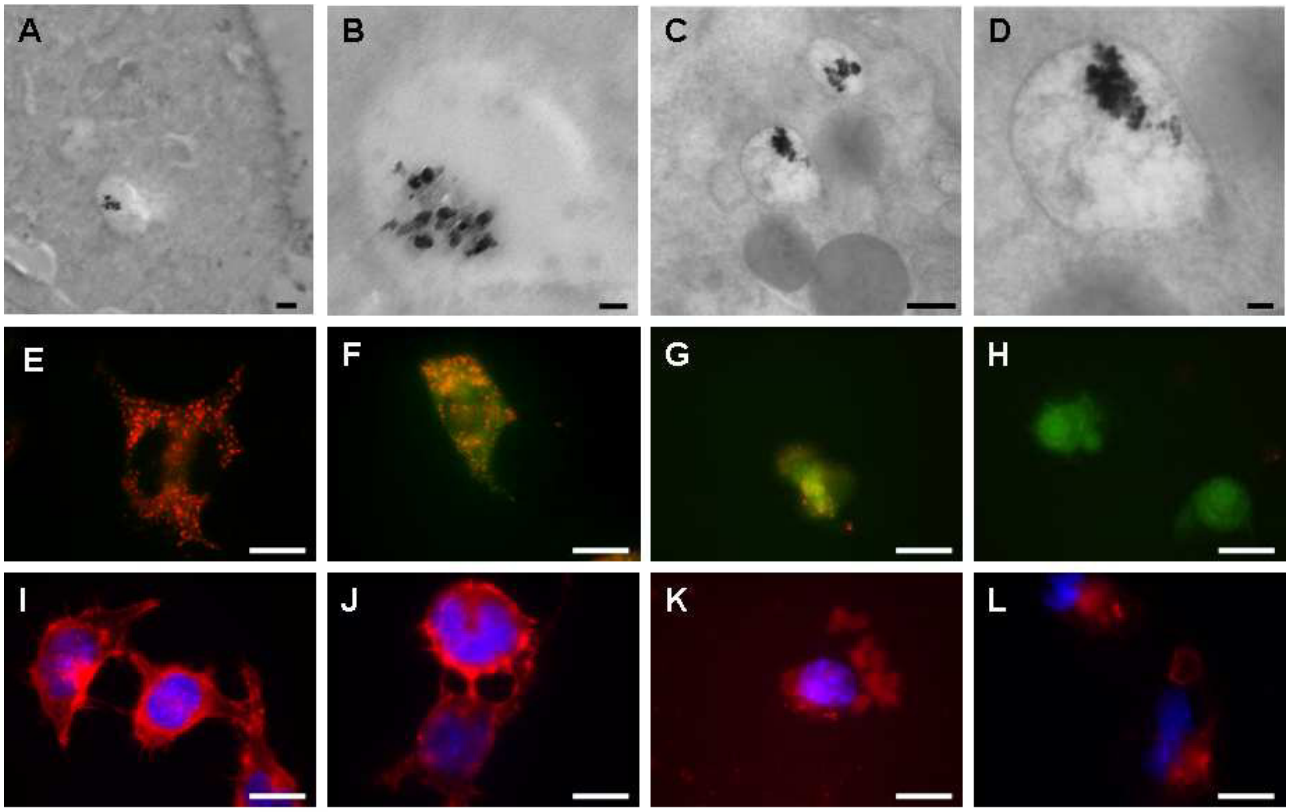

Figure 4. Subcellular effects of Ag nanoparticles at a concentration of 25 μg ml^{-1} for 24 h. ((A)–(D)) Demonstration of internalization and localization of Ag nanoparticles to intracellular vacuoles in N2A cells with transmission electron microscopy (TEM) after 24 h of incubation with 25 μg ml^{-1} of Ag nanoparticles in cell culture. (A) Ag25; (B) higher magnification image of (A); (C) Ag25Disp; and (D) higher magnification of lower intracellular vacuole in (C). The scale bars are ((A), (C)) 500 nm and ((B), (D)) 100 nm. ((E)–(L)) Representative images of N2A cell interactions with or without 25 μg ml^{-1} of Ag nanoparticles or 2.5 μg ml^{-1} CdO after 24 h. ((E)–(H)) Fluorescent microscopy, demonstrating mitochondrial membrane permeability. ((I)–(L)) Fluorescent microscopy for cytoskeletal architecture. ((E), (I)) Control; ((F), (J)) Ag25Disp; ((G), (K)) Ag25; ((H), (L)) CdO. ((E)–(L)) The scale bars are 20 μm.

To investigate the potential role of oxidative stress after 24 h of cell exposure to the Ag nanoparticles, the increase in fluorescent intensity of the probe DCFH compared to control cells was observed. Increases in cell fluorescence are expressed as an n-fold increase relative to control cells, which are equal to 1-fold. Therefore, an increase in cell fluorescence indicates an increase in the generation of reactive oxygen species (ROS) or oxidative stress to the cells (figure 5(C)). Cells incubated with Ag25 nanoparticles show dose-dependent increases in ROS generation up to approximately 1.5–2 times the control, with significant increases at 50–100 μg ml^{-1} concentrations (figure 5(C)). However, the Ag25Disp nanoparticles do not induce a significant increase in ROS compared to the control until the highest concentration of 100 μg ml^{-1}. The positive control for the generation of ROS was hydrogen peroxide (H_2O_2), which shows a dose-dependent linear correlation ($R^2 = 0.9986$) in ROS production from cells incubated with concentrations from 0 to 2000 μM, indicating the validity of the assay (figure 5(D)). Further, the endogenous ability of the Ag nanoparticles to react with the DCFH probe in an acellular environment and produce fluorescence indicative of ROS was also investigated and found to be negative (data not shown).

To study the effect of Ag nanoparticles on cell growth, N2A cells were treated with NGF over five days. As expected, NGF induced a significant increase in cell proliferation compared to the control cells (figure 5(E)). However, there was a significant decrease in cell viability after long-term culture with the Ag nanoparticles when compared to the 24 h exposure for the Ag nanoparticles. In addition, after 24 h, the Ag25Disp showed less toxicity than the Ag25 nanoparticles, yet after five days of exposure to the nanoparticles there is no difference in toxicity between the Ag25Disp and Ag25 nanoparticles. Furthermore, the presence of NGF in the cultures did not rescue cell viability. Based on this data, it is hypothesized that the stability of nanoparticle coating (i.e. polysaccharide) must be addressed since there is a change in cytotoxicity over time for the different Ag25Disp and Ag25 nanoparticles. Additionally, the NGF signaling pathway appears to be disrupted by the presence of Ag nanoparticles and this loss could be a result of the Ag nanoparticles interacting or interfering with key signaling proteins that mediate the NGF pathway in the N2A cells.

4. Discussion

The plasmonic nature of noble metal nanoparticles, such as silver, is useful for imaging and the development of bionanoprobes if used at non-toxic concentrations. Many

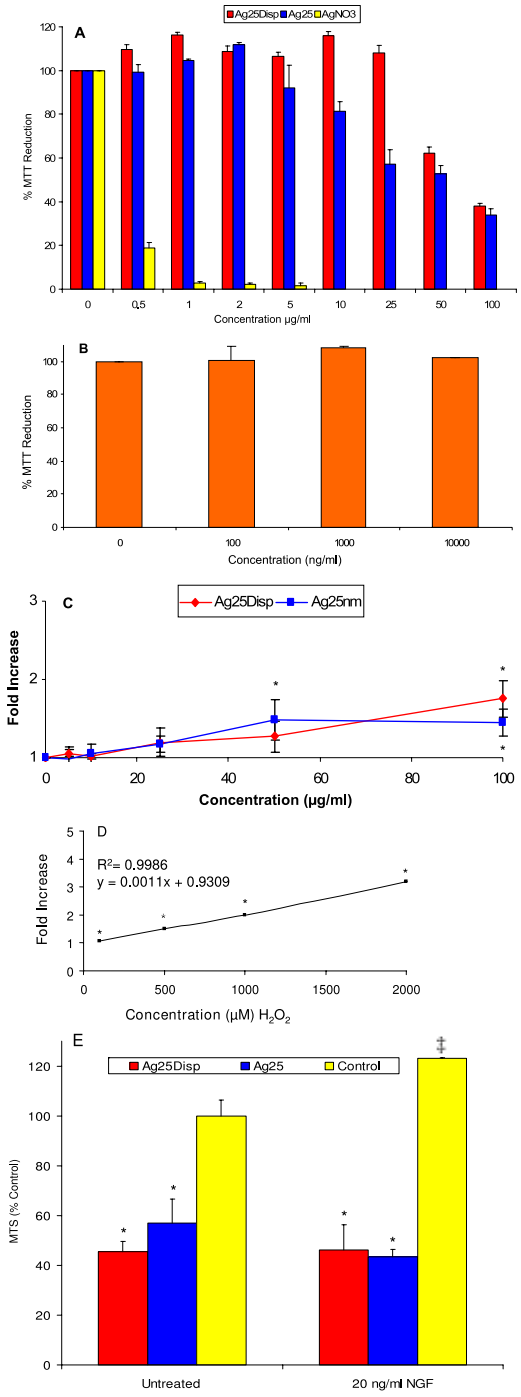

Figure 5. Biocompatibility assessment of cells incubated with Ag nanoparticles. ((A)–(B)) MTT cell viability assay after 24 h. (A) Ag nanoparticles and positive control silver nitrate ($AgNO_3$), (B) high viability after incubation with ng ml^{-1} concentrations of polysaccharide alone to demonstrate the biocompatibility of the coating on Ag25Disp nanoparticles, (C) assessment of ROS generation after incubation with Ag nanoparticles for 24 h. (D) Validity of ROS assay with positive control hydrogen peroxide. (E) N2A cell proliferation after five days of treatment with Ag nanoparticles and nerve growth factor (NGF). Notice that both forms of Ag nanoparticles display reduced proliferation and that the addition of NGF does not mitigate the response. All experiments were performed in at least triplicate, with * indicating a significant decline in cell proliferation ($p < 0.05$) from the control, while ‡ indicates a significant increase in proliferation ($p < 0.05$) from the control.

groups are pursuing metal-based nanoparticles as biolabels that are designed to target the surface of certain cell types or specific areas within individual cells for applications in imaging and cancer therapies (Danscher and Stoltenberg 2006, Siiman *et al* 2000, Lochner *et al* 2003, Dahan *et al* 2003, Kumar *et al* 2007). In the case of targeted cancer cell or tumor destruction, the photodynamic properties of silver nanoparticles may be considered useful, but the surrounding healthy tissues should be protected from damage. Therefore, the history of metals in neurodegenerative disease must be weighed against the benefits of the therapy when oxidative stress has been shown with *in vitro* experiments (Hussain *et al* 2005).

In this study, we showed that low concentrations (<25 $\mu g\ ml^{-1}$) of Ag nanoparticles can effectively provide biological labeling in live cells due to their intense plasmon-resonant properties that can be readily detected by a high illumination system. The Ag nanoparticles coated with a biocompatible polysaccharide readily bind to the surface of living cells while allowing the maintenance of normal cell morphological features such as neurite extensions. However, mitochondrial membrane integrity and actin cytoskeletal structure appear to be disrupted, with a concurrent elevation in ROS, after 24 h of incubation, so in future studies lower concentrations would be preferred. In addition, nerve growth factor has been shown to be important in inducing neuronal proliferation (Blanco *et al* 2001), and here we show that, regardless of nanoparticle coating, both types of Ag nanoparticle were able to disrupt NGF-induced proliferation over time. Furthermore, the growth curve study also provided evidence that over time the biocompatibility that was seen in the polysaccharide-coated Ag nanoparticles is lost, and this potentially is a result of the coating being degraded by the cell.

By administering a critical, low concentration of Ag nanoparticles, the physical blockage of cellular functions occurring after internalization or binding to the plasma membrane may be avoided as well as the prevention of extracellular protein or nutrient binding between the nanoparticles and cell culture media. It is still suspected that nanoparticle agglomeration in cell culture media may prevent effective uptake into the cell as well as the lack of transport into the nuclear region. The lack of internalization into the nucleus was expected because passive transport into the nucleus is limited to particles with diameters of 9 nm or less, and the primary size of the Ag nanoparticles used in this study was as small as 10 nm, but the majority of the Ag nanoparticles were 30–40 nm in diameter (Paine *et al* 1975). Another factor to consider in the development of biolabels is the mechanism of uptake, which can vary by cell type. Recently, we have shown that there are distinct differences in the uptake mechanism and cell viability results after exposure to nanomaterials in neuroblastoma cells compared to alveolar macrophages (Schrand *et al* 2007b). More importantly, the long-term effects of the Ag nanoparticles on cellular functions due to surface or internal accumulation (reaching a detrimental saturation) or degradation of surface coatings in certain environments (i.e. endosomes, lysosomes) is still not known, but this study illustrates that over time the biocompatibility seen with a

surface coating can change. Additional factors to consider for the optimization of Ag nanoparticles as biological labels include modifications to their size, shape, functionalization, and concentration for targeted applications.

5. Conclusions

In this study, we demonstrated that low concentrations of Ag nanoparticles ($<25\ \mu g\ ml^{-1}$) become bound to the plasma membranes of live cells, and intensely scattered light when imaged at submicron resolution with high illumination light microscopy, thereby opening the possibility for their potential use as biological labels. The tailorability of the Ag nanoparticles through surface engineering lends itself to a greater variety of *in vivo* applications such as imaging agents (Lesniak *et al* 2005), products for wound healing (Poon and Burd 2004, Fong and Wood 2006), and the development of cancer therapies (Zharov *et al* 2005, Wieder *et al* 2006). Therefore, taking advantage of the highly desirable properties of Ag nanoparticles while protecting the body from harmful side effects is a worthwhile long-term goal, and surface modification of nanoparticles seems to be one of the keys to achieving that goal.

Acknowledgments

AMS received funding from the Biosciences and Protection Division, Air Force Research Laboratory, under the Oak Ridge Institute for Science and Education (ORISE) and the Dayton Area Graduate Studies Institute (DAGSI). LKB-S received funding through a Post-Doctoral Fellowship from the National Research Council. We acknowledge United States Air Force Academy students Jonathan Stralka and Ryan Teets for their great effort and participation in the cell culture and toxicity studies. DLS and ZP measurements were kindly provided by Michael Moulton, with funding through the Biosciences and Protection Division, Human Effectiveness Directorate, Air Force Research Laboratory under the Oak Ridge Institute for Science and Education and STEP Program.

References

Alberts B, Johnson A, Lewis J, Raff M, Bray D, Hopkin K, Roberts K and Walter P 2004 *Essential Cell Biology* 2nd edn (New York, NY: Garland Science) (in English) http://en.wikipedia.org/wiki/Endosomes.

Alt V, Bechert T, Steinrücker P, Wagener M, Seidel P, Dingeldein E, Domann E and Schnettler R 2004 An *in vitro* assessment of the antibacterial properties and cytotoxicity of nanoparticulate silver bone cement *Biomaterials* **25** 4383–91

Balogh L, Swanson D R, Tomalia D A, Hagnauer G L and McManus A T 2001 Dendrimer-silver complexes and nanocomposites as antimicrobial agents *Nano Lett.* **1** 18–21

Bellamy L J 1975 *The Infrared Spectra of Complex Molecules* (London: Chapman and Hall)

Berry C C, Wells S, Charles S, Aitchison G and Curtis A S G 2004 Cell response to detran-derivatised iron oxide nanoparticles post internalization *Biomaterials* **25** 5405–13

Berry C C, Wells S, Charles S and Curtis A S G 2003 Dextran and albumin derivatised iron oxide nanoparticles: influence on fibroblasts *in vitro Biomaterials* **24** 4551–7

Blanco V, Camelo J L and Carri N G 2001 Growth inhibition, morphological differentiation, and stimulation of survival in neuronal cell type (Neuro-2A) treated with trophic molecules *Cell Biol. Int.* **25** 909–17

Braydich-Stolle L, Hussain S, Schlager J J and Claude-Hofmann M 2005 *In vitro* cytotoxicity of nanoparticles in mammalian germline stem cells *Toxicol. Sci.* 1–8

Carmichael J, DeGraff W D, Gazdar A F, Minna J B and Mitchell J B 1987 *Cancer Res.* **47** 936–42

Chen C *et al* 2005 Multihydroxylated [Gd@C82(OH)22]n nanoparticles: antineoplastic activity of high efficiency and low toxicity *Nano Lett.* **5** 2050–7

Chou W-L, Yu D-G and Yang M-C 2005 The preparation and characterization of silver-loading cellulose acetate hollow fiber membrane for water treatment *Polym. Adv. Technol.* **16** 600–7

Coates J 2000 *Interpretation of Infrared Spectra, A Practical Approach in Encyclopedia of Analytical Chemistry* ed R A Meyers (Chichester: Wiley) pp 10815–37

Cool D R, Fenger M, Snell C R and Loh Y P 1995 Identification of the sorting signal motif within pro-opiomelanocortin for the regulated secretory pathway *J. Biol. Chem.* **270** 8723–9

Cool D R, Normant E, Shen F, Chen H C, Pannel L, Zhang Y and Loh Y P 1997 Carboxypeptidase E is a regulated secretory pathway sorting receptor: genetic obliteration leads to endocrinological disorders in the Cpefat mouse *Cell* **88** 1–11

Dahan M, Levi S, Luccardini C, Rostaing P, Riveau B and Triller A 2003 *Science* **302** 442–5

Danscher G and Stoltenberg M 2006 *Prog. Histochem. Cytochem.* **41** 57–139

Dumortier H, Lacotte S, Pastorin G, Marega R, Wu W, Bonifazi D, Brian J-P, Prato M, Muller S and Bianco A 2006 Functionalized carbon nanotubes are non-toxic and preserve the functionality of primary immune cells *Nano Lett.* **6** 1522–8

Foley S *et al* 2002 Cellular localisation of a water-soluble fullerene derivative *Biochem. Biophys. Res. Commun.* **294** 116–9

Fong J and Wood F 2006 Nanocrystalline silver dressings in wound management: a review *Int. J. Nanomedicine* **1** (4)

Foster B 2004 Focus on microscopy: a technique for imaging live cell interactions and mechanisms *Am. Lab.* **11** 21–7

Gupta A K and Curtis A S G 2004 Lactoferrin and ceruloplasmin derivatized superparamagnetic iron oxide nanoparticles for targeting cell surface receptors *Biomaterials* **25** 3029–40

Gupta A K and Gupta M 2005 Synthesis and surface engineering of iron oxide nanoparticles for biomedical applications *Biomaterials* **26** 3995–4021

Hoshino A, Kujioka F, Oku T, Suga M, Sasaki Y F, Ohta T, Yasuhara M, Suzuki K and Yamamoto K 2004 Physicochemical properties and cellular toxicity of nanocrystal quantum dots depend on their surface modification *Nano Lett.* **4** 2163–9

Hummel D O 1982 *Atlas of Polymer and Plastics Analysis* 2nd completely revised edition (Deerfield Beach, FL: Verlag Chemie International) (v.1, Polymers, structures and spectra. v.2, Plastics, fibres, rubbers, resins; starting and auxiliary materials, degradation products. v.3, Additives and processing aids)

Hussain S M and Frazier J M 2002 *Toxicol. Sci.* **69** 424–32

Hussain S M, Hess K L, Gearhart J M, Geiss K T and Schlager J J 2005 *In vitro* toxicity of nanoparticles in BRL-3A rat liver cells *Toxicol. In Vitro* **19** 975–83

Hussain S, Javorina A, Schrand A, Duhart H, Ali S and Schlager J 2006 The interaction of manganese nanotubes with PC-12 cells induces dopamine depletion *J. Toxicol. Sci.* **92** 456–63

Jendelova P *et al* 2004 Magnetic resonance tracking of transplanted bone marrow and embryonic stem cells labeled by iron oxide nanoparticles in rat brain and spinal cord *J. Neurosci. Res.* **76** 232–43

Jeong S H, Hwang Y H and Yi S C 2005 Antibacterial properties of padded PP/PE nonwovens incorporating nano-sized silver colloids *J. Mater. Sci.* **40** 5413–8

Jordan A, Scholz R, Wust P, Schirra H, Schiestel T, Schmidt H and Felix R 1999 Endocytosis of detran and silan-coated magnetite nanoparticles and the effect of intracellular hyperthermia on human mammary carcinoma cells *in vitro J. Magn. Magn. Mater.* **194** 185–96

Kedar N P 2003 Can we prevent Parkinson's and Alzheimer's disease? *J. Postgrad. Med.* **49** 236–45

Kumar S, Harrison N, Richards-Kortum R and Sokolov K 2007 Plasmonic nanosensors for imaging intracellular biomarkers in live cells *Nano Lett.* **7** 1338–43

Lesniak W, Bielinska A U, Sun K, Janczak K W, Shi X, Baker J R Jr and Balogh L P 2005 *Nano Lett.* **5** 2123–30

Lochner N, Pittner F, Wirth M and Gabor F 2003 *J. Control. Release* **89** 249–59

Murdock R C, Braydich-Stolle L, Schrand A M, Schlager J J and Hussain S M 2008 Characterization of nanomaterial dispersion in solution prior to *in vitro* exposure using dynamic light scattering technique *Toxicol. Sci.* **101** 239–53

Paine P L, Moore L C and Horowitz S B 1975 Nuclear envelope permeability *Nature* **254** 109–14

Poon V K M and Burd A 2004 *Burns* **30** 140–7

Schrand A M, Dai L, Schlager J J, Hussain S M and Ōsawa E 2007b Differential biocompatibility of carbon nanotubes and nanodiamonds *Diamond Relat. Mater.* **16** 2118–23

Schrand A M, Huang H, Carlson C, Schlager J J, Ōsawa E, Hussain S M and Dai L 2007a Are diamond nanoparticles cytotoxic? *J. Phys. Chem.* B **111** 2–7

Siiman O, Gordon K, Burshteyn A, Maples J A and Whitesell J K 2000 *Cytometry* **41** 298–307

Skebo J E, Grabinski C M, Schrand A M, Schlager J J and Hussain S M 2007 Assessment of metal nanoparticle agglomeration, uptake, and interaction using a high illuminating system *Int. J. Toxicol.* **26** 135–41

Sondi I, Goia D V and Matijevic E 2003 Preparation of highly concentrated stable dispersions of uniform silver nanoparticles *J. Colloid Interface Sci.* **260** 75–81

Suvorova E I, Klechkovskaya V V, Kopeikin V V and Buffat P A 2005 Stability of Ag nanoparticles dispersed in amphiphilic organic matrix *J. Cryst. Growth* **275** 2351–6

Vainrub A, Pustovyy O and Vodyanoy V 2006 Resolution of 90 nm ($\lambda/5$) in an optical transmission microscope with an annular condenser *Opt. Lett.* **31** 2855–7

Vodyanoy V 2005 High resolution light microscopy of live cells *Microsc. Today* **13** (May) 26–8

Wang H and Joseph J A 1999 *Free Radic. Biol. Med.* **27** 612–6

Wieder M E, Hone D C, Cook M J, Handsley M M, Gavrilovic J and Russell D A 2006 *Photobiol. Sci.* **5** 727–34

Wilhelm C, Billotey C, Roger J, Pons J N, Bacri J-C and Gazeau F 2003 Intracellular uptake of anionic superparamagnetic nanoparticles as a function of their surface coating *Biomaterials* **24** 1001–11

Yeo S Y, Lee H J and Jeong S H 2003 Preparation of nanocomposite fibers for permanent antibacterial effect *J. Mater. Sci.* **38** 2143–7

Zharov V P, Galitovskaya E N, Johnson C and Kelly T 2005 *Lasers Surg. Med.* **37** 219–26